Materials Science & Engineering A 737 (2018) 401–412

Contents lists available at ScienceDirect

Materials Science & Engineering A

journal homepage: www.elsevier.com/locate/msea

Effect of plastic deformation on the ageing behaviour of an Al–Cu–Mg alloy with a high Cu/Mg ratio

Ivan Zuiko*, Rustam Kaibyshev

Belgorod State University, Pobeda 85, Belgorod 308015, Russia

ARTICLE INFO

Keywords:
Aluminium alloys
Thermomechanical processing
Mechanical properties
Precipitation
Deformation structure
Ageing

ABSTRACT

The effect of tensile strain ranging from 1% to 7% on the decomposition sequence and mechanical properties of an AA2519 alloy with low Si content is studied. Pre-straining promotes the precipitation of θ′- and Ω-phases at dislocations and suppresses the precipitation of GP-zones and θ″-phase. The aspect ratio (AR) of the homogeneously nucleated Ω_I-phase is higher than that of the Ω_{II}-phase nucleated on the θ′-phase/Al interfaces by a factor of ~ 4. Replacement of θ″-phase by a dispersion of θ′- and Ω-phases took place under peak-ageing condition and thus imparted only a minor hardening effect, despite a seven-fold increase in the volume fraction of the strengthening precipitates. An increase in the yield stress by 30% with increasing pre-strain from 1% to 7% is attributed to an increase in the lattice dislocation density. Over-ageing leads to replacement of the Ω_{II}-phase by the θ′-phase.

1. Introduction

Al–Cu–Mg alloys with a high Cu/Mg ratio are used as armor plates and components in aerospace due to their excellent combination of strength and ductility [1,2]. The superior mechanical properties of the AA2519 alloy, which belongs to this system, are achieved through thermomechanical processing (TMP), which involves solution treatment, cold working by rolling or stretching and subsequent artificial ageing [1–4]. Minor Mg addition to an Al–Cu solid solution results in a complex ageing behaviour [3–5], including the classic precipitation sequence wherein transition phases have plate-like shapes and $\{001\}_\alpha$ habit planes:

$$SSSS \rightarrow GP{-}zones\,(Al_3Cu) \rightarrow \theta''\,(Al_3Cu) \rightarrow \theta'(Al_2Cu) \rightarrow \theta(Al_2Cu) \quad (1)$$

as well as a decomposition sequence that provides the precipitation of the transition Ω-phase with $\{111\}_\alpha$ habit planes:

$$SSSS \rightarrow \{111\}\,clusters \rightarrow \Omega(Al_2Cu) \rightarrow \theta{-}phase \quad (2)$$

where SSSS is a supersaturated solid solution, the Guinier-Preston (GP) zones are single layers of pure Cu atoms on $\{001\}_\alpha$ planes, the θ″-phase with coherent broad faces is comprised of two $\{001\}_{Cu}$ layers separated by three $\{001\}_\alpha$ planes, the θ′-phase has a bct structure with coherent broad faces along the $\{100\}_{Al}$ planes and semi-coherent interfaces at their peripheries, the θ-phase is the thermodynamic equilibrium form of Al_2Cu with a bct lattice and incoherent interfaces, and the Ω phase having orthorhombic lattice forms as thin hexagonal-shaped plates [1,6–11]. The Ω-phase does not appear to nucleate at dislocations in Ag-free Al–Cu–Mg alloys [1,5,7,8,12,13]. However, cold-working before artificial ageing strongly affects the number density and volume fraction of the Ω-phase [3,9,14,15]. Importantly, the origin of the Ω-phase in Ag-free Al–Cu–Mg alloys with high Cu/Mg ratios (e.g., AA2519) remains unknown [3,4,7,8,12,14].

Superposition of the Mg additions and pre-straining before artificial ageing have a beneficial effect on the strength and ductility of an Al–5 wt%Cu alloy [14,16]. However, the origin of this positive effect is still poorly understood, despite numerous reports that examine the precipitation behaviour and mechanical properties of Al–Cu–Mg alloys with Cu/Mg ratios ≥ 5.6 [3–5,14,16–19]. It is known [1,7,8,11,14,16,20–23] that the addition of specific micro-alloying elements can significantly improve the precipitation-hardening response of Al–Cu alloys and simultaneously provide an increase in their strength and ductility. This is commonly believed to be caused by the complex influence of these micro-elements on the number density and morphology (i.e., diameter-to-thickness aspect ratio) of plate-shaped precipitates, as well as their nucleation on the $\{111\}_\alpha$ planes in addition to the $\{001\}_\alpha$ habit planes. N. Ünlü et al. suggested [14] that the superior properties of pre-strained Al–Cu alloys with trace additions of Mg were associated with an increased volume fraction of the Ω-phase; in turn, the latter effect was attributed to inducing precipitation Sequence

* Corresponding author.
E-mail addresses: zuiko_ivan@bsu.edu.ru (I. Zuiko), rustam_kaibyshev@bsu.edu.ru (R. Kaibyshev).

https://doi.org/10.1016/j.msea.2018.09.017
Received 18 June 2018; Received in revised form 6 September 2018; Accepted 7 September 2018
Available online 08 September 2018
0921-5093/

(2) due to the enhanced dislocation density [14]. The aim of the present study is to establish the role of trace additions of Mg and pre-strain in achieving high strength for an AA2519 alloy.

It is known [5,14,16,24–26] that additions of Si inhibits precipitation of the Ω-phase and no precipitation of the Ω-phase occurs in Al–Cu alloys with trace additions of Mg if the Mg/Si ratio (wt%) is < 3. This deleterious effect is attributed to the high binding energy between Si and Mg, which leads to the formation of Si-Mg clusters, restricting the Mg available for nucleation of the Ω-phase [5,14,27]. No precipitation of the Ω-phase was detected in an AA2519 grade alloy with Mg/Si~1.5 in the peak-aged condition [4]. In the present study, the AA2519 alloy with Mg/Si ~ 23 is examined to reveal the role of pre-straining in the precipitation of the Ω-phase.

2. Material and experimental procedures

AAn AA2519 alloy, with a nominal chemical composition of Al–5.64Cu–0.33Mn–0.23Mg–0.15Zr–0.11Ti–0.09V–0.08Fe–0.08Zn–0.04Sn–0.01Si (in weight %) was manufactured by semi-continuous casting followed by homogenization annealing at 510 °C for 24 h [3,5,28]. Billets with dimensions of 55 × 120 × 155 mm^3 were machined from ingots and swaged at a temperature of ~400 °C up to final dimensions of 41 × 155 × 160 mm^3. The standard flat "dog-bone" shaped tensile test specimens with a cross-section of 3 × 7 mm^2 and a 25 mm gauge length were cut from the central part of the billets. The specimens were solution annealed at 530 °C for 1 h and then immediately quenched in cold-water (~ 20 °C). For T8-type tempering, the specimens were pre-strained by tension at room temperature to 1%, 3% and 7% elongation for the T81, T83 and T87 conditions, respectively, and then subjected to final ageing at 190 ± 1 °C for different durations. In addition, a programmable furnace Memmert Universal Oven model UF55 was used to simulate differential scanning calorimetry (DSC) conditions. The un-strained specimens as well as the specimens pre-strained to 1% or 7% were heated to 85 °C at a heating rate of 2 °C/min, soaked for 1 h and finally water-quenched.

Vickers microhardness was measured in the electro-polished gauge section of the pre-strained specimens using a Wilson Wolpert 402MVD tester operating at a load of 2 N with a dwell time of 10 s. Repeatability of the results was ensured by testing more than 12 independent indentations for each data point. The maximum and minimum values were discarded, and the remaining 10 readings were used to determine the average values and standard deviations of microhardness for each condition.

The pre-stretching procedure and uniaxial tensile tests to failure were carried out at ambient temperature using an Instron 5882 screw-driven testing machine with a constant crosshead speed of 2 mm/min providing an initial strain rate of 1.3×10^{-3} s^{-1}. To minimize end effect during tension tests, the load frame was equipped with an automatic high-resolution contacting extensometer MFX 500. Yield stress (σ_{YS}), ultimate tensile strength (σ_{UTS}), uniform elongation (ε_u) and elongation-to-failure (δ) were determined in accordance with ASTM E-8 standard. To ensure the reliability of the tensile tests, at least three specimens were tested for each studied material condition.

DSC was performed using an SDT Q600 (TA Instruments) calorimeter. The mass of the DSC samples was approximately 55 mg, and an inert atmosphere of pure argon was used. The solutionized (and subsequently water-quenched) samples were heated from 20 to 600 °C at a rate of 2 °C/min together with pure aluminium. The time between water-quenching and the onset of the DSC measurements was 20 min.

Transmission-electron-microscopy (TEM) studies were carried out after ageing at 85 and 190 °C. Thin foils for TEM were produced by a twin-jet electro-polishing method. JEOL JEM-2100 and Technai G^2 F20 microscopes were operated at an accelerating potential of 200 kV were used. Further details about the TEM and orientation imaging microscopy (OIM) studies have been described elsewhere [3,5,28]. To improve the image contrast of the examined precipitates, the electron beam was carefully aligned with < 100 > α and < 011 > α zone axes. A schematic of the ideal diffraction patterns for both zone axes are summarized in Fig. 1. In the figure, the reflections used for dark-field (DF-TEM) imaging are denoted by an orange circle. The interpretation of the diffraction patterns with streaks from GP zones, θ″-phase and reflections from the θ″-phase was provided in previous work [3]. The θ′- and Ω-phase platelets were easily identified using their characteristic diffraction spots at 1/2g = < 220 > Al and 1/3 and 2/3g = < 220 > Al, respectively [3,7,29]. Calculations of the average true diameter, D_T, and average true thickness, W, of the platelets for these two phases was carried out with a high accuracy in the < 100 > α and < 011 > α zone axes at exact focus. At the < 001 > α zone axis, two variants of the edge-on precipitates of the θ′-phase with $\{100\}_\alpha$ habit planes are clearly visible in the bright-field (BF) image, while the third orientation appeared face-on and is almost invisible. This third variant of the θ′-phase is visible in BF-image in the < 011 > α zone axis. Two variants of the Ω-phase with $\{111\}_\alpha$ habit planes located along the < 010 > Ω and < 310 > Ω directions are visible in the < 011 > Al zone axis and appeared as hexagonal plates in the projected image [9,15,29,30]. The dimensions of four different variants of the Ω-phase platelets were found to be essentially the same, and the D_T and W values were calculated for the < 011 > α zone axis in the present study only.

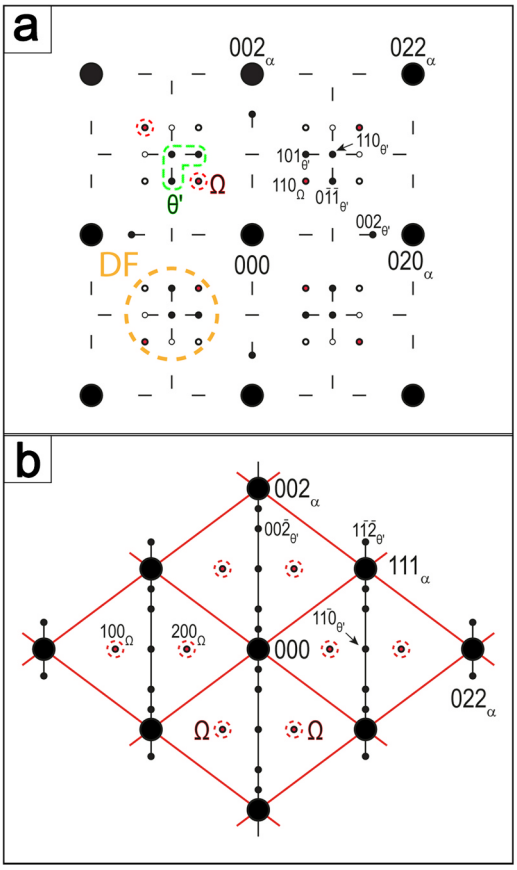

Fig. 1. Schematic of the diffraction patterns for < 100 > α (a) and < 011 > α (b) zone axes. Red- and green colours indicate the θ′- and Ω-phases, respectively. (For interpretation of the references to color in this figure legend, the reader is referred to the web version of this article.)

The number density, N_V, of the θ′- and Ω-phases with plate-like shapes was calculated as [3,5,15,22,30–32]: $N_V = \frac{N_T}{A_S(t+D_T)}$, where N_T is the total number of precipitates, defined as follows: $N_T = N\left(1+\frac{t+D_T}{C\sqrt{A_S}}\right)$. The coefficient, C, is equal to the number of variants in the counting area. The coefficient C takes into account the number of invisible

variants in the count area and is equal to 1/2 and 1 for $\{001\}_{Al}$ and $\{111\}_{Al}$ precipitates, respectively [9,22]. A_S is the area on the micrograph where the N precipitates were counted. The D_T value was determined from the measured diameter, D_M, as follows: $D_M = \frac{t+\frac{\pi}{4}D_T}{t+D_T}D_T$. The total volume fraction, f_V, of both-types of plates within the grain/subgrain interiors was calculated by multiplying the average particle volume and number density per unit volume: $f_V = \frac{N_V \pi D_T^2 W}{4}$, where W is the average thickness of the precipitates. The number of calculated particles was $\geq 10^3$ for the material under each condition. The foil thickness in the beam direction, t, was determined by convergent beam electron diffraction method using Kossel-Möllenstedt fringes under two-beam condition [3,32,33].

Similar to previous work [28], the dislocation density was evaluated by the Williamson-Hall method.

3. Results

3.1. Microstructure

Hot forging followed by solution treatment resulted in the formation of a partially recrystallized microstructure with an average grain size of ~16 μm and dislocation density of $1 \pm 0.4 \times 10^{14}$ m^{-2} (Fig. 2a). The tension had no significant effect on the grain shape (not shown). The pre-strains of 1%, 3% and 7% provided an increase in the dislocation density by factors of 2.5, 6 and 7, respectively (Fig. 2b).

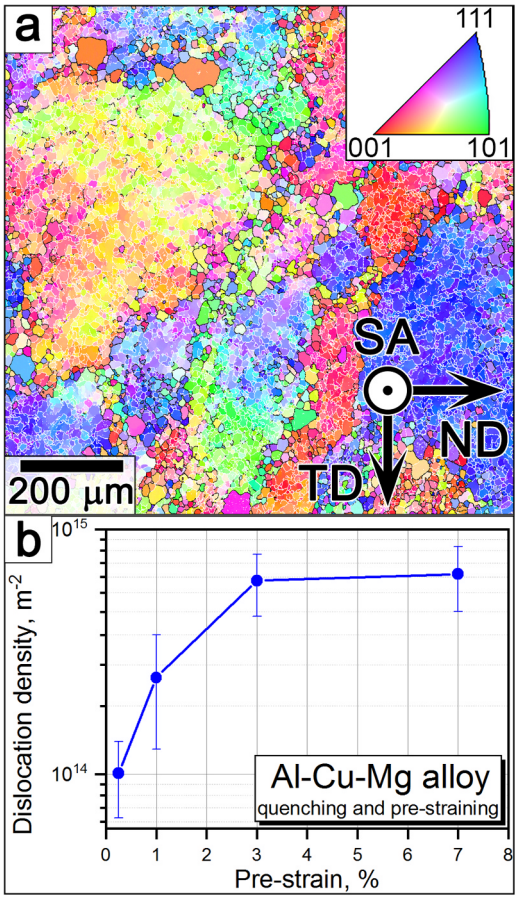

Fig. 2. Representative OIM map of the microstructures produced after solution treatment (a), and the effect of pre-straining on the dislocation density (b). (For interpretation of the references to color in this figure legend, the reader is referred to the web version of this article.)

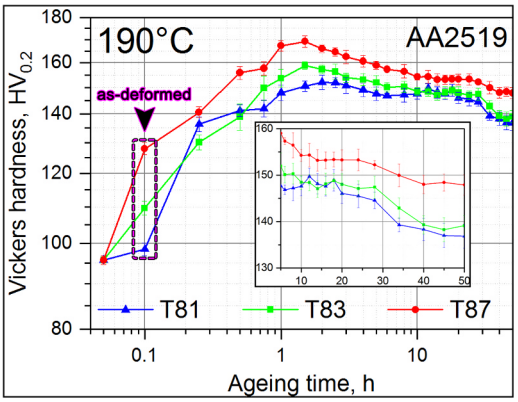

Fig. 3. Age-hardening curves demonstrating the evolution of the Vickers microhardness as a function of increasing pre-strain and ageing time at 190 °C. (For interpretation of the references to color in this figure legend, the reader is referred to the web version of this article.)

3.2. Mechanical properties

As follows from Fig. 3, tensile strains of 1%, 3% and 7% increased the microhardness from 96 ± 1 to 99 ± 2, 110 ± 2 and 128 ± 2 $HV_{0.2}$, respectively. The ageing behaviour of the material that was pre-strained to 1% was found to be largely similar to that of the non-strained material [5]. A 52% increase in microhardness occurs within 1 h. A peak of 150 ± 2 $HV_{0.2}$ appears after 2 h followed by a plateau to 30 h with a microhardness of 147 ± 2 $HV_{0.2}$ (Fig. 3). Upon further ageing, the hardness decreases remarkably (see inset in Fig. 3). A distinct hardness peak of 160 ± 2 $HV_{0.2}$ appears after pre-straining by 3% with 1.5 h ageing. This microhardness value is typical for an AA2519T87 alloy [17,34]. Further ageing results in softening down to 149 ± 2 $HV_{0.2}$ and 135 ± 2 $HV_{0.2}$ after 10 and 35 h, respectively. After pre-straining by 7%, the peak hardness is 170 ± 2 $HV_{0.2}$. Upon further ageing the hardness decreases to 150 ± 3 $HV_{0.2}$ after 10 h indicating over-ageing occurred. Thus, the present AA2519 alloy exhibits higher hardness than other grades of this alloy with Mg/Si ~ 5 [17].

Typical engineering stress-strain (σ–ε) curves after pre-straining and peak-ageing are shown in Fig. 4. The relevant mechanical properties, including microhardness, σ_{YS}, σ_{UTS}, ε_U, δ, and the σ_{YS}/σ_{UTS} ratio (attributed to work-hardening rate) are summarized in Table 1. T87 tempering provides a 44% increase in σ_{YS} and, 15% increase in σ_{UTS} in comparison to T6 tempering; ductility slightly decreases [5]. It is worth noting that pre-straining has almost no effect on Tabor's $c \sim 2.8$ value in the relationship $\sigma_{UTS} = c \times HV$ [5,35]. The AA2519T87 alloy exhibits a 20% increase in σ_{YS}, 10% increase in σ_{UTS} and 30% increase in ductility in comparison to the AA2219T87 alloy [34].

Strain hardening, represented by the σ_{YS}/σ_{UTS} ratio and slope on true stress-true strain curves, decreases with increasing pre-straining, which leads to decreasing uniform elongation. However, the elongation-to-failure remains almost unchanged. The main impact of pre-straining on the σ–ε curves is the transition from continuous yielding [36,37] in T6 condition to discontinuous one in T87 condition. It is worth noting that the σ–ε curves of AA2519 subjected to intense rolling exhibit only continuous yielding even at $\sigma_{YS} > 500$ MPa [28]. The σ–ε curves after tension without ageing exhibit continuous yielding, followed by jerky flow that is associated with heterogeneous localization of plastic deformation within the bulk of a material and is referred as the Portevin-Le Chatelier (PLC) effect [36–39]. The mechanism of the PLC phenomenon is ascribed to dynamic strain ageing (DSA) [36–39]. Segregation of the solutes on dislocations occurs during plastic deformation. Ageing completely eliminates the PLC effect and decreases the strain hardening and, therefore, provides depletion of major portion of the solutes from Al matrix.

Analysis of Fig. 4 and Table 2 shows that 1%, 3% and 7% straining

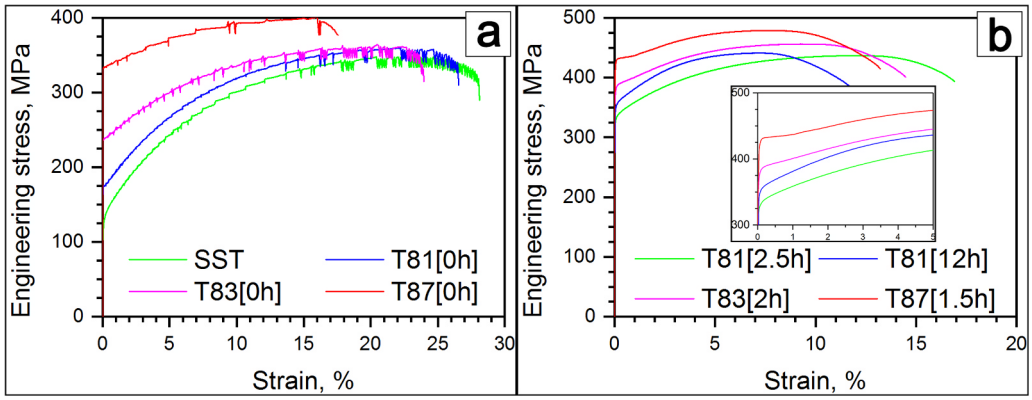

Fig. 4. Typical engineering stress-strain (σ–ε) curves for the AA2519 alloy at different processing states: (a) only pre-stretching, (b) pre-strain followed by peak ageing. Inset in (b) shows enlarged section of the σ–ε curves. The number in square brackets means ageing duration. (For interpretation of the references to color in this figure legend, the reader is referred to the web version of this article.)

without ageing provides a 33%, 75% and 146% increase, respectively, in σ_{YS} and has only a minor effect on ductility. These values are significantly higher than those provided by pre-strain followed by peak ageing. Peak ageing provides a 96% (175 MPa), 65% (159 MPa) and 26% (87 MPa) increase in σ_{YS} after pre-straining by 1%, 3% and 7%, respectively. Therefore, the increase in the pre-strain from 1 to 7% approximately halves the increment in σ_{YS} during subsequent ageing. At pre-strains ≥ 3%, the effect of ageing on σ_{UTS} is ≤ 100 MPa.

3.3. DSC analysis

The measured DSC plots are summarized in Fig. 5. Precipitation reactions revealed by DSC of the AA2519 alloy without pre-straining are described in detail in companion work [5]. The main feature of the AA2519 alloy with low Si and without pre-strain is the formation of Cu-Mg co-clusters and GP zones at 71 °C followed by the continuous GP → θ″-phase transformation between 103 and 201 °C [5]. Increasing the pre-strain hinders the formation of Cu-Mg clusters and GP zones; the precipitation of the transition phases is shifted to lower temperature (Fig. 5). A pre-strain of 1% decreases the energy released during the formation of Cu-Mg co-clusters and GP-zones by a factor of ~ 7, and shifts this reaction to a higher temperature by ΔT ~ 14K. Pre-straining above 3% completely suppresses the formation of Cu-Mg co-clusters and GP-zones and their subsequent transformation to the θ″-phase. In the un-strained AA2519 alloy, the exothermic peaks associated with precipitation of the Ω- and θ′-phases are located at 203 and 242 °C, respectively, and therefore, they are distinctly different from each other [5]. The energy released during precipitation of the θ′-phase is higher by a factor of ~ 20 than that released during precipitation of the Ω-phase [5]. After 3% pre-straining, however, both of these exothermic reactions merge into a single peak at 200 °C with an energy of 11.7 J g^{-1} released. Therefore, pre-strains ≥ 3% induce simultaneous precipitation of the Ω- and θ′-phases. 7% pre-straining also shifts this peak to 195 °C. Moreover, increasing the pre-strain provides a ~ 3 K reduction in the melting point of material.

Table 2
Tensile properties of AA2519 after pre-straining and natural ageing for ~ 15 min.

Pre-strain (%)	σ_{YS}, MPa	σ_{UTS}, MPa	Elongation %		σ_{YS}/σ_{UTS}
			ε_U	δ_T	
1	179 ± 2.5	353 ± 3	23 ± 1.5	27 ± 1.5	0.51
3	240 ± 2	365 ± 2	21 ± 1	24 ± 0.8	0.66
7	336 ± 2	403 ± 2	17 ± 0.5	18 ± 0.4	0.8

3.4. Precipitation structure

3.4.1. Effect of pre-strain on precipitation at 85 °C

TEM observations of AA2519 annealed at 85 °C are summarized in Fig. 6. In the material that experienced no pre-strain, distinct coherent GP-zones with an average dimension of ~ 2 nm were found (Fig. 6a). These zones exhibit specific contrast, which is attributed to strong elastic strain fields in the BF-TEM images and produces distinct continuous streaks parallel to the $< 001 >_{\alpha}$ directions through the $\{200\}_{\alpha}$ spots in the diffraction patterns [3,5,7,40,41] (Fig. 6a). As seen in Fig. 6b, 1% pre-strain strongly reduces the number density of the GP-zones, and only weak evidence of the formation of solute clouds on dislocations was found. After 7% pre-straining, no evidence for the formation of GP-zones was observed (Fig. 6c). Therefore, the TEM data also indicated suppression of GP-zones nucleation by pre-straining, which is in agreement with the DSC measurements discussed in the previous section.

3.4.2. Effect of pre-strain on precipitation at 190 °C

3.4.2.1. Under-ageing. The uniform precipitation of GP-zones/θ″-phase particles and nucleation of the θ′-phase on dislocations were detected

Table 1
Mechanical properties of AA2519 after pre-straining followed by ageing at 190°C. Data for AA2219 and AA2519 without pre-strain are also shown for comparison.

Alloy	Temper		Ageing time, h	Hardness, $HV_{0.2}$	σ_{YS}, MPa	σ_{UTS}, MPa	Elongation %		σ_{YS}/σ_{UTS}
							ε_U	δ_T	
AA2519	T6 [12]	II	12	149 ± 2	292 ± 1	409 ± 2	15 ± 0.6	16 ± 1	0.75
	T81	I	2.5	152 ± 2	346 ± 2	432 ± 3	12 ± 0.2	17 ± 0.3	0.8
		II	12	150 ± 2	357 ± 3	436 ± 2	8 ± 0.2	12 ± 0.3	0.82
	T83		2	157 ± 2	395 ± 3	460 ± 3	9 ± 0.5	15 ± 1.4	0.86
	T87		1.5	169 ± 2.5	421 ± 1	471 ± 1	8 ± 0.5	13 ± 0.5	0.89
AA2219 [34]	T81/T83		-	-	325	425	-	7	0.77
	T87		-	-	350	430	-	10	0.81

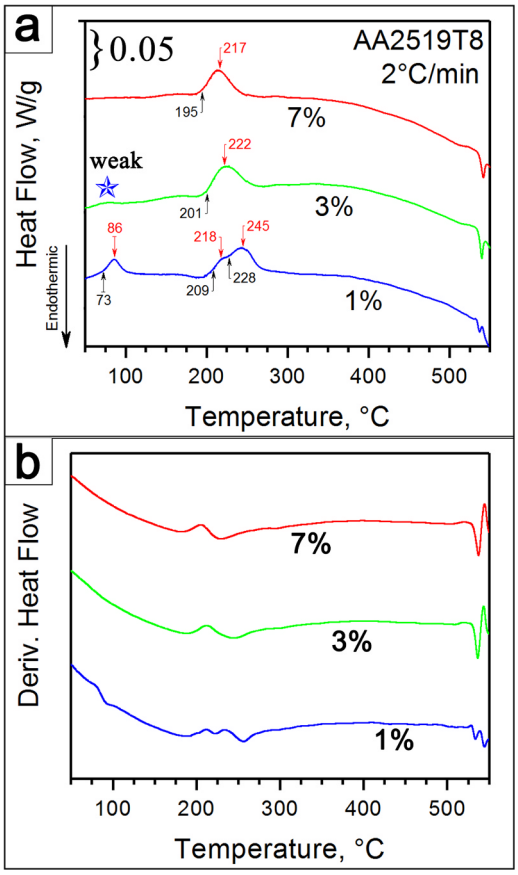

Fig. 5. DSC measurements: heat-flow diagrams (a) and derivatives (b). The black and red arrows indicate the reaction onset and peak temperatures, respectively. The blue star denotes a relatively weak reaction. (For interpretation of the references to color in this figure legend, the reader is referred to the web version of this article.)

after pre-straining by 1% followed by ageing at 190 °C for 0.5 h (Fig. 7a). Strong discontinuous $< 001 >_{\alpha}$ streaks through the {200} and {220} matrix spots on SAED patterns are indicative of the θ″-phase precipitation [3,5,7], which was found to be dominant in the microstructure. Continuous diffuse streaks parallel to the $< 001 >_{\alpha}$ directions through the $\{200\}_{\alpha}$ spots were attributed to GP-zones. Precipitation of the θ′-phase was evidenced by the spots at the $\{110\}_{\alpha}$ positions and four adjacent streaks corresponding to the $\{110\}_{\alpha}$ spots (cf. Figs. 1a and 7a) [3,5,7]. There was also distinct evidence of the θ′-phase in BF-images taken at the $< 011 >_{\alpha}$ zone axes condition (Figs. 1b and 7b). In addition, the Ω-phase platelets inhabiting $\{111\}_{\alpha}$ nucleated homogeneously, as seen in the BF-images taken at the $< 011 >_{\alpha}$ zone axis condition, although SAED patterns contained no characteristic reflections from this phase due its low number density (Fig. 7b, Table 3).

Increasing the pre-strain suppressed the formation of the GP zones and increased the volume fraction of the θ′- and Ω-phases. After 3% pre-straining, discontinuous streaking along $< 001 >$ directions through {200} matrix spots was found (Fig. 7c), which indicated precipitation of θ″-phase. Distinct diffraction spots arisen from the θ′-phase were detected in the SAED patterns taken along $< 100 >_{\alpha}$ and $< 011 >_{\alpha}$ zone axes (Figs. 1, 7c and 7d). Precipitation of the Ω-phase gave rise to diffusive streaking through $\{111\}_{\alpha}$ in addition to the aforementioned characteristic diffraction spots (Fig. 7d and f) [7]. After 7% pre-straining, the volume fraction of the θ″-phase became low and discontinuous streaking through the $\{200\}_{\alpha}$ spots could be rarely observed (Fig. 7e). The θ′-phase became the dominant phase (Fig. 7c and e). The proportion of the Ω-phase was nearly trebled (Table 3); distinct

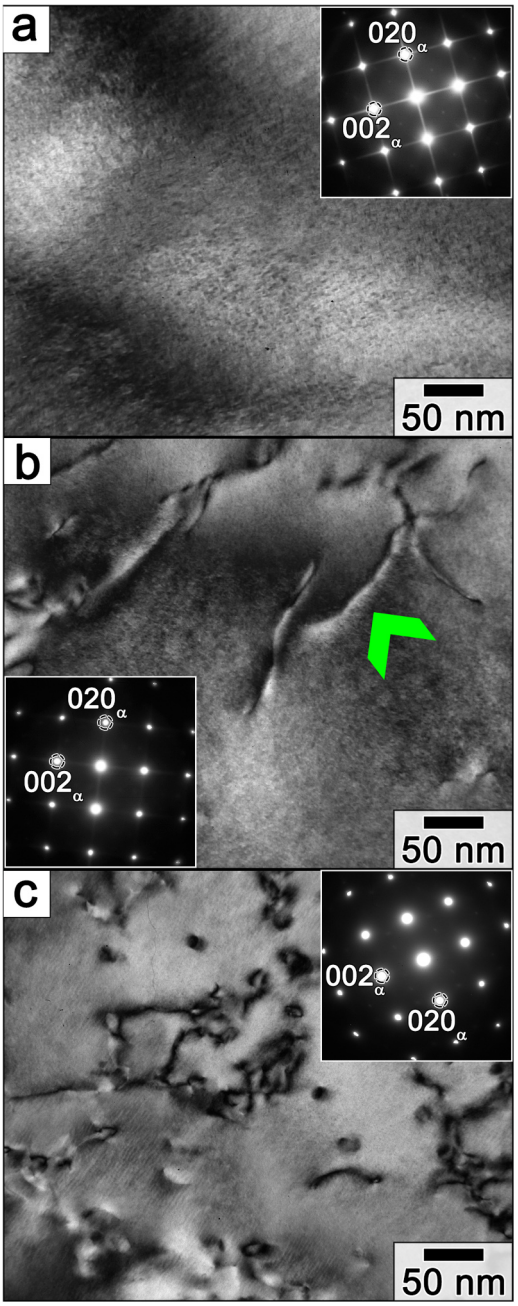

Fig. 6. BF-TEM micrographs and corresponding SAED patterns showing the effect of pre-straining on precipitation patterns developed after ageing at 85 °C for 1 h: un-strained material (a), 1% pre-straining (b), and 7% pre-straining (c). In (b), the green arrow exemplifies a precipitation-free zone at a dislocation. (For interpretation of the references to color in this figure legend, the reader is referred to the web version of this article.)

diffusive streaking through $\{111\}_{\alpha}$ was observed in the SAED pattern taken at the $< 011 >_{\alpha}$ zone axis (Fig. 7f). A major portion of the Ω-phase nucleates homogeneously in the α-Al matrix, while some platelets of this phase nucleate at the edges of the θ′-phase (Fig. 7f). The platelets of this phase were characterized by their relatively low length-to-diameter aspect ratio, and are referred to as the Ω_{II}-phase throughout the manuscript. In addition to the main strengthening precipitates, a fairly small amount of the precipitates from (α + S)-phase field [7] was found occasionally.

3.4.2.2. Peak ageing. Peak ageing leads to the dissolution of GP zones and to an increase in the volume fraction of the θ′-phase by a factor of

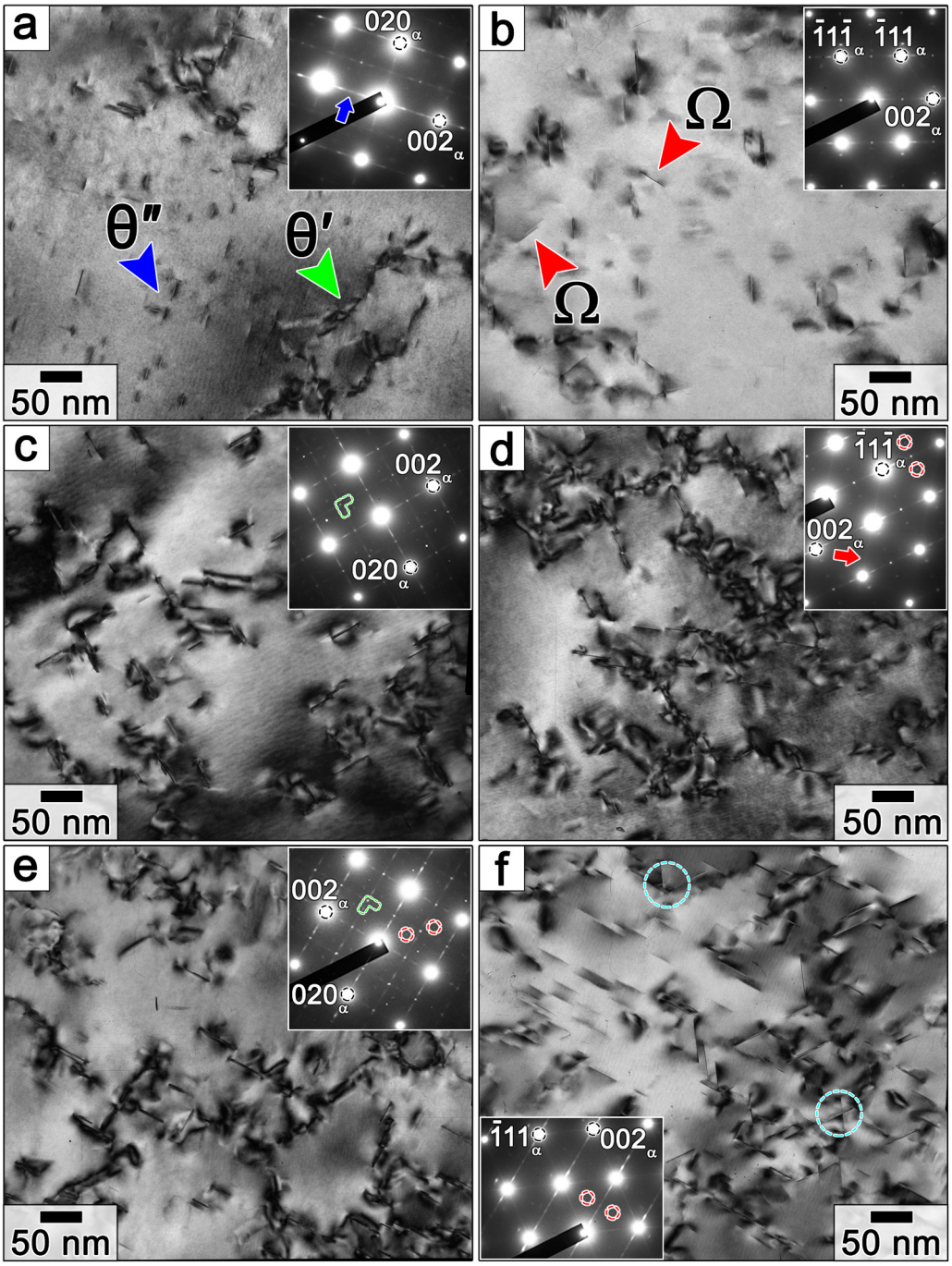

Fig. 7. BF-TEM images and corresponding SAED patterns after underageing (0.5 h at 190 °C) following pre-strains of 1% (a, b), 3% (c, d) and 7% (e, f) taken along the $< 001 >_\alpha$ (a, c, e) and $< 011 >_\alpha$ (b, d, f) zone axes. Red circles in the SAED of d, e and f are indicative for 1/3 and 2/3 $[220]_\alpha$ positions and sky blue circles in BF-image f) show the Ω-phase nucleated at the edge interfaces of the θ′-platelets. (For interpretation of the references to color in this figure legend, the reader is referred to the web version of this article.)

~3 at the expense of the θ″-phase with pre-strain (Fig. 8a, c, e, Table 4). The diameter of the θ′-phase platelets increases with prolonged ageing (Table 4). As a result, the increase in the number density of the θ′-phase after peak ageing is relatively low in comparison with the under-aged material (Table 4). Under the peak-ageing condition, increasing the pre-strain leads to replacement of the θ″-phase by the θ′-phase (Fig. 8a, c, e, Table 4). Platelets of the θ″-phase, which precipitated homogeneously in dislocation-free zones, showed strong coherent elastic stresses around all interfaces. No continuous diffusive streaks were observed on the SAED pattern taken at the $< 100 >_\alpha$ zone axis condition after any pre-straining and, therefore, no evidence for GP zones was found. The θ″-phase platelets produced discontinuous $< 100 >_\alpha$ streaks through the $\{200\}_\alpha$ positions, as well as spot reflections at the $\{220\}_\alpha$ positions (Fig. 8a and b) [3]. The spots positions were attributed to the θ″-phase in the measured SAED patterns, and those in the diffraction pattern simulated by using the Gerold model [3,7] were nearly the same. Therefore, the distinct superlattice of the θ″-phase appears, and its stoichiometry is Al_3Cu [5,7]. After pre-strain of 1%, the θ″-phase became dominant (Fig. 8a). Areas of the θ″-phase are delimited by areas of the θ′-phase nucleated on dislocations. After a pre-strain of 3%, the number densities of the θ″-phase and θ′-phase are nearly the same (Fig. 8c). After a pre-strain of 7%, the θ′-phase is

Table 3
Geometric dimensions, number density and volume fraction of the Ω-phase after different heat treatments. UAC, PAC and OAC refer to the under-, peak- and over-ageing conditions, respectively.

Temper	Pre strain, %	Condition	Aging time, h	Mean plate dimensions, nm		Aspect ratio	Number density $\times 10^{20}$, #/m^{-3}	Volume fraction, %
				Diameter	Thickness			
T6	0	UAC	0.5	26 ± 12	0.8 ± 0.10	33	-	-
		PAC #2	12	117 ± 68	1 ± 0.2	120	1.2 ± 1.8[a]	0.08 ± 0.07
T8	1	UAC	0.5	33 ± 12	0.9 ± 0.20	39	5.6 ± 3.6	0.03 ± 0.01
		PAC #1	2.5	47 ± 24	0.8 ± 0.2	58	4 ± 3	0.06 ± 0.04
		PAC #2	12	141 ± 81	1.2 ± 0.3	119	0.5 ± 0.3	0.08 ± 0.02
	3	UAC	0.5	36 ± 12	0.8 ± 0.2	47	4.8 ± 1.7	0.04 ± 0.01
		PAC	2	44 ± 20	0.95 ± 0.26	46	11 ± 4	0.14 ± 0.05
	7	UAC	0.5	34 ± 13	0.8 ± 0.2	40	16 ± 0.3	0.11 ± 0.04
		PAC	1.5	40 ± 18	1 ± 0.3	37	23 ± 10	0.3 ± 0.12
		OAC	12	48 ± 18	1.2 ± 0.3	40	3.6 ± 1.5	0.1 ± 0.06

[a] Non-homogeneous distribution of plates.

dominant (Fig. 8e). The volume fraction of the θ′-phase is nearly independent of the pre-strain, despite the fact that its number density increases by a factor of ~4 after a pre-strain of 7% (Table 3). Pre-strain ≥3% strongly decreases the diameter of the θ′-phase platelets because of the transition from near homogeneous nucleation [5,42,43] during peak-ageing without pre-strain to the strong dominance of nucleation on dislocations [6,7] (Fig. 8e). As a result, AR of this phase decreases by factors of ~ 2 and ~ 3 after pre-strains of 3% and 7%, respectively.

Peak-ageing provides a two- or threefold increase in the volume fraction of the Ω-phase, as compared to under-ageing (Table 3). In turn, pre-straining increases the volume fraction and number density of the Ω-phase by factors of ~4 and ~19, respectively (Fig. 8b, d, f, Table 3). As a result, after pre-strains of 3 and 7% the four characteristic spots appear around the $\{011\}_\alpha$ position, as well as streaking along $<111>_\alpha$ are observed in $<011>_\alpha$ SAED patterns. It is worth noting that the dimensions of the Ω-phase in the AA2519 alloy and a modified AA2139 alloy [9] after different pre-strains followed by peak-ageing are essentially the same. After peak-ageing without pre-strain, the Ω_I-phase platelets exhibit AR~120 (Table 3) [5] and are located uniformly in the Al matrix. Under the peak ageing condition, increasing pre-strain strongly decreases the AR of the Ω-phase by a factor of ~ 4, providing a high number density (Table 3). At a pre-strain of 1%, precipitation of the Ω-phase with medium AR occurs homogeneously during peak-ageing (Fig. 8a, Table 3). Increasing the ageing time to 12 h leads to an increase in the length of the Ω-platelets; AR approaches ~120 (Fig. 9a, Table 3). It is apparent that only particles of the Ω_I-phase with a high AR > 100 remain.

This strong effect of pre-straining on a Ω-phase dispersion is attributed to promotion of Ω_{II}-platelets nucleation on the θ′-phase/Al interfaces (Fig. 10c). It is apparent that the Ω-phase nucleates on the edge interfaces of the θ′-phase. Next, these two phases concurrently grow (Fig. 9b). As mentioned above, nucleation of the θ′-phase on dislocations becomes the main nucleation mechanism of this phase with pre-strains ≥ 3%, and therefore, nucleation of the Ω_{II}-phase on the θ′-phase/Al interfaces also becomes a major nucleation mechanism. At a pre-strain of 7%, this mechanism provides a high volume fraction of the Ω-phase after peak-ageing (Fig. 8f, Table 3). It is worth noting that the formation of clusters was also observed on $\{111\}_\alpha$ planes (red arrows in Fig. 10c). Therefore, homogeneous nucleation of the Ω_I-phase and heterogeneous nucleation of the Ω_{II}-phase on θ′-phase/Al interfaces occurs concurrently at pre-strains ≥ 3%. Over-ageing leads to replacement of the Ω_{II}-phase nucleated on θ′-phase/Al interfaces by the θ′-phase (Fig. 9, Table 3). As a result, the average diameter and AR of the Ω-phase slightly increases and the number density and volume fraction decreases by factors of ~ 6 and ~ 3, respectively (Fig. 9b, Table 3). Notably, after a pre-strain of 1%, nucleation of the Ω-phase on platelets of the θ′-phase was occasionally found (Figs. 8b, 10a and b). However, there was no difference in the dimensions of the Ω-phase that was nucleated homogeneously and the θ′-phase/Al interfaces after a pre-strain of 1%. This difference appears at pre-strains ≥ 3%, where a major portion of the θ′-phase was nucleated on dislocations, and therefore, a major portion of the Ω-phase nucleates on the θ′-phase/Al interfaces.

Segregation of Mg was detected at the Ω-phase peripheries (Fig. 11), which is in agreement with previous reports [10,44,45]. Quantitative EDX analysis revealed that the content of Mg (positions 2 and 3) is higher than that in the Al matrix (position 1) by a factor of ~ 4 (Fig. 11). It can therefore be inferred that Mg addition is essential for the nucleation of the Ω-phase which exhibits distinct coherent strain fields.

In addition to the aforementioned phase a fairly small amount of lath-shaped S′-precipitates [7,46,47] could observed under all conditions (not shown here). We found a single S′-Al_2CuMg with a $\{210\}_\alpha$ habit plane located along $<100>_\alpha$ in one of ~ 20 examined micrographs. In addition, θ_{II}' precipitates with $\{110\}_\alpha$ habit plane [8] was also found (yellow arrow in Fig. 8d). Volume fraction of aforementioned concomitant phases is negligible. Therefore, S′- and θ_{II}'-phases are unimportant to the mechanical properties of the AA2519 alloy.

4. Discussion

4.1. Effect of pre-strain on precipitation sequence

Pre-strain disrupts the clustering process and hinders precipitation of GP-zones at low temperatures. The formation of GP-zones and the θ″-phase was found in the underaged state at a relatively high temperature of 190 °C. It was recently shown [5,48,49] that minor Mg addition may profoundly change the nature of the precipitates formed in the Al matrix and on the dislocations. The addition of 0.1 at% Mg is sufficient for segregation at almost all dislocations if the lattice dislocation density is ~ $2{\cdot}10^{14}$ m^{-2} [48]. Therefore, segregations of Cu and Mg appears on major parts of the dislocations, even after a pre-strain ≥ 3%. As a result, trace Mg additions could not promote the precipitation of GP zones [5]. Cottrell clouds hinder the homogeneous precipitation of GP zones and the θ″-phase. At 190 °C, partial disruption of Cu-Mg clouds on dislocations occurs, and GP zones on the $\{001\}_\alpha$ planes and Cu-Mg clusters on the $\{111\}_\alpha$ planes precipitate. During ageing, the GP zones dissolve due to the formation of θ″- and θ′-phases with lower energies [11], in accordance with the Gibbs-Thomson free energy diagram [6]. In contrast, $\{111\}_{Al}$ clusters are retained and served as pre-cursors for the homogeneous nucleation of the Ω_I-phase.

In addition, the Cottrell Cu-Mg clouds raise the Cu content, approaching a Al_2Cu stoichiometric composition and strongly promoting the nucleation of the θ′-phase on lattice dislocations because pre-straining induces the formation of dense and uniform dislocation structure. As a result, pre-straining promotes a transition from the

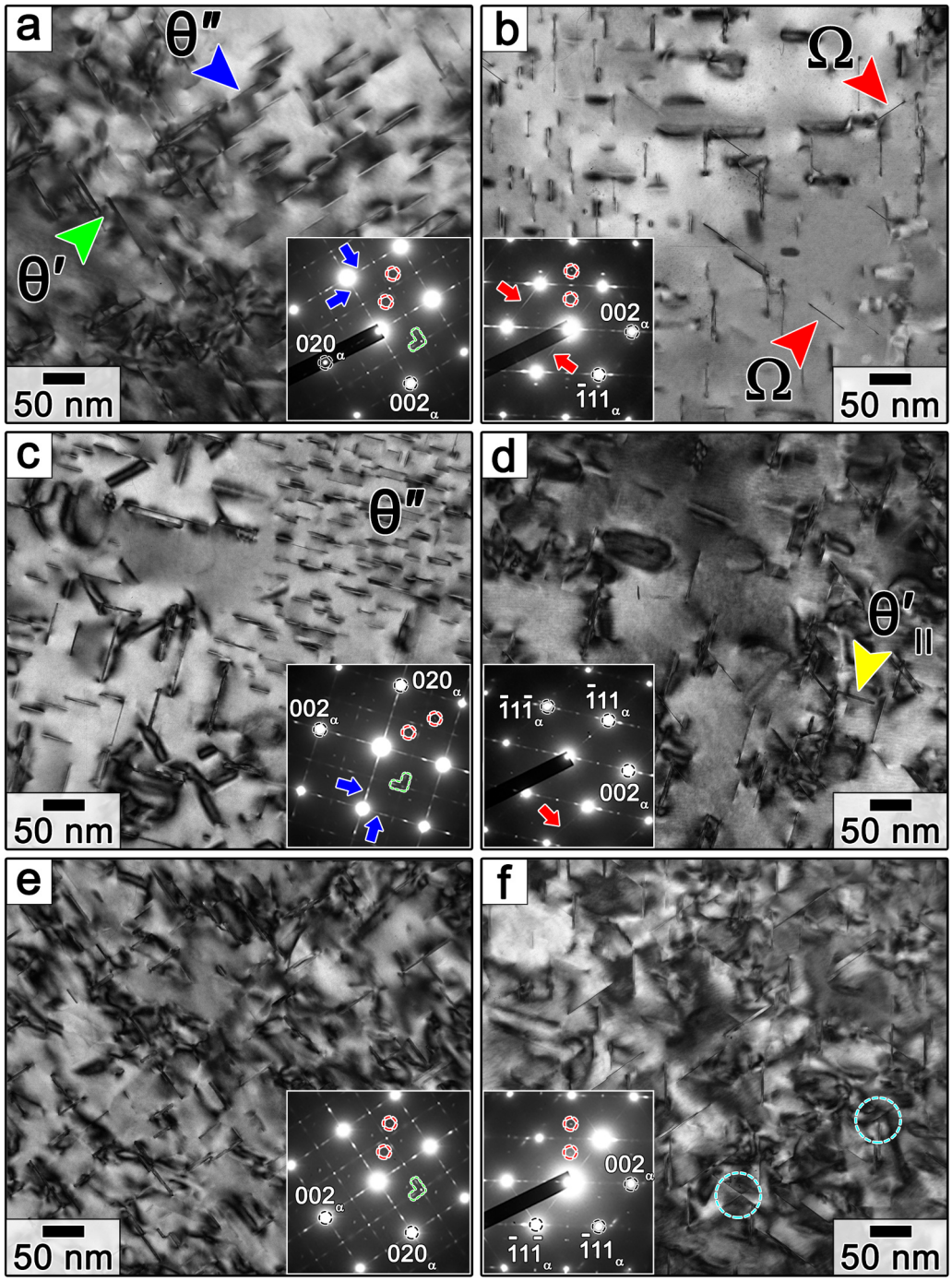

Fig. 8. BF-TEM micrographs and corresponding SAED patterns with a $< 100 >_\alpha$ (a, c, e) and $< 011 >_\alpha$ (b, d, f) zone axes after peak-ageing at 190 °C following a pre-strain of 1% (2.5 h) (a, b), 3% (2 h) (c, d) and 7% (1.5 h) (e, f). (For interpretation of the references to color in this figure legend, the reader is referred to the web version of this article.)

Table 4
Dimensions, number density and volume fraction of the θ′-phase after different heat treatments.

Temper	Pre strain, %	Condition	Aging time, h	Mean plate dimensions, nm		Aspect ratio	Number density $\times 10^{20}$, #/m^{-3}	Volume fraction, %
				Diameter	Thickness			
T6[a]	0	PAC	12	132.2 ± 76.6	4.45 ± 1.22	29.7	3.96 ± 0.32	2.37 ± 0.92
T8	3	PAC	2	49.2 ± 23.2	3.04 ± 0.82	16.1	28.33 ± 0.84	1.74 ± 0.20
	7	PAC	1.5	34.5 ± 16.5	2.97 ± 0.86	11.6	60.13 ± 0.73	2.09 ± 0.63
		OAC	12	34.3 ± 14.4	3.32 ± 1.03	10.3	56.90 ± 0.10	2.04 ± 0.08

[a] From previous work [5]

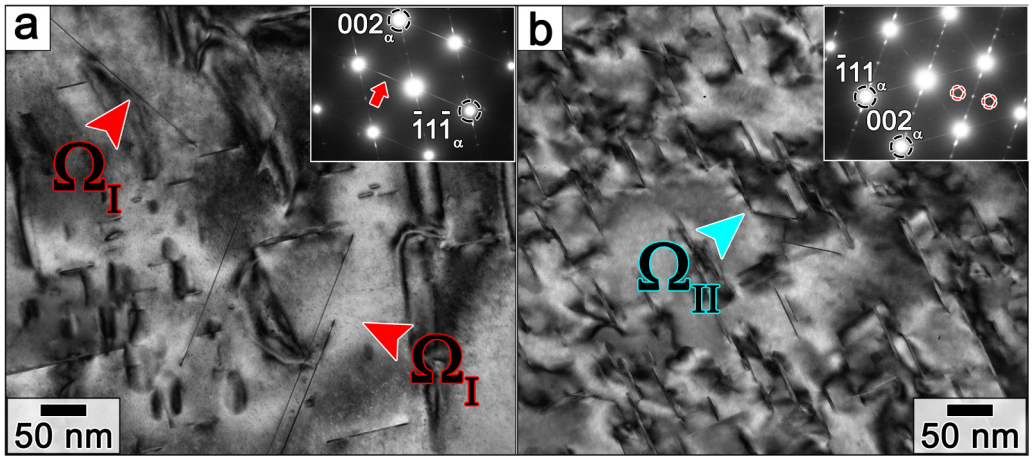

Fig. 9. BF-TEM micrographs with corresponding SAED patterns recorded near the $< 011 >_\alpha$ zone axes after pre-strains of 1% (a) and 7% (b) followed by ageing 190°C for 12 h. The image clearly demonstrates the difference in size between the homogeneously nucleated Ω_I-phase (red arrows) and Ω_{II}-phase (sky blue arrow) nucleated on the θ′-phase/Al matrix interface. Red circles denote reflexes from the Ω-phase. (For interpretation of the references to color in this figure legend, the reader is referred to the web version of this article.)

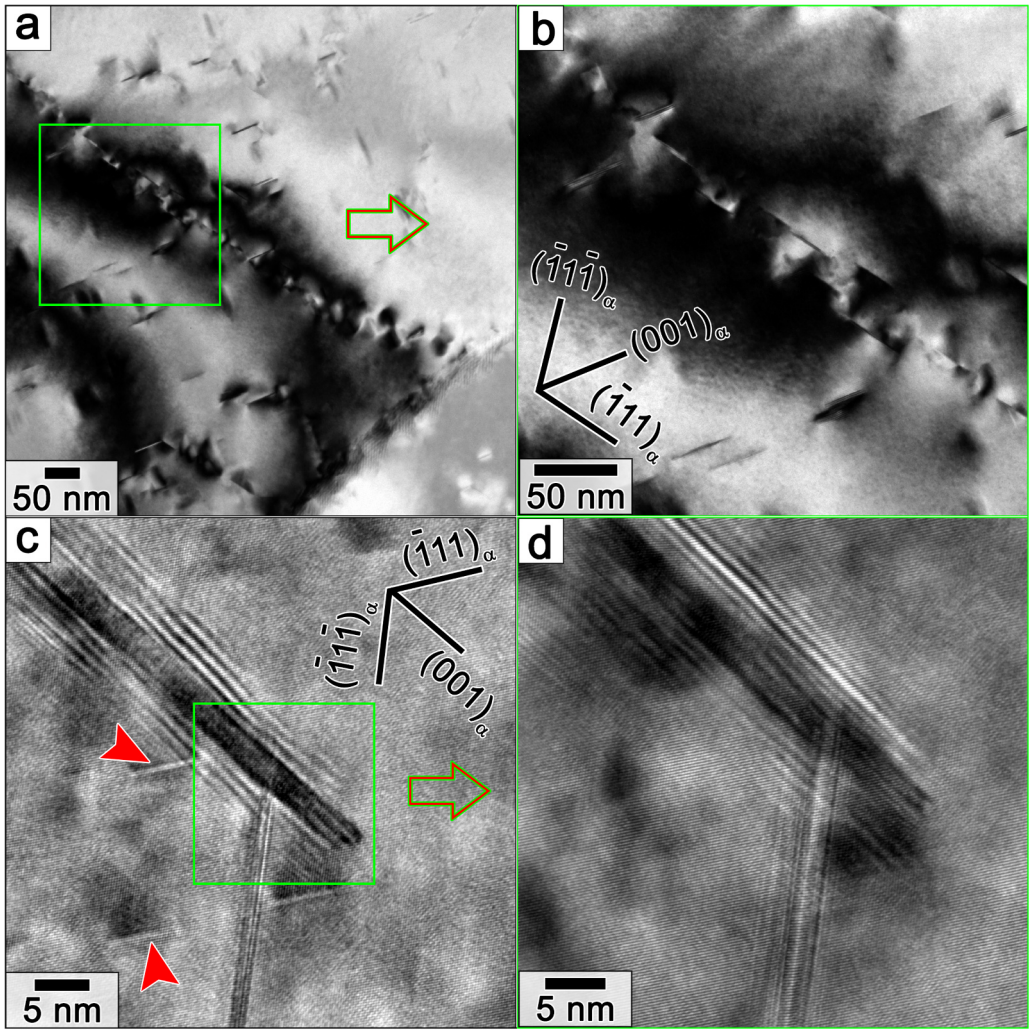

Fig. 10. Formation of the Ω-phase chains in the AA21519 after a pre-strain of 1% followed by ageing at 190 °C for 0.5 h (a, b). Nucleation of Ω-phase on θ′-phase/Al interfaces after a pre-strain of 7% followed by ageing at 190 °C for 12 h (c, d), red arrows indicate $\{111\}_{Al}$ clusters. (For interpretation of the references to color in this figure legend, the reader is referred to the web version of this article.)

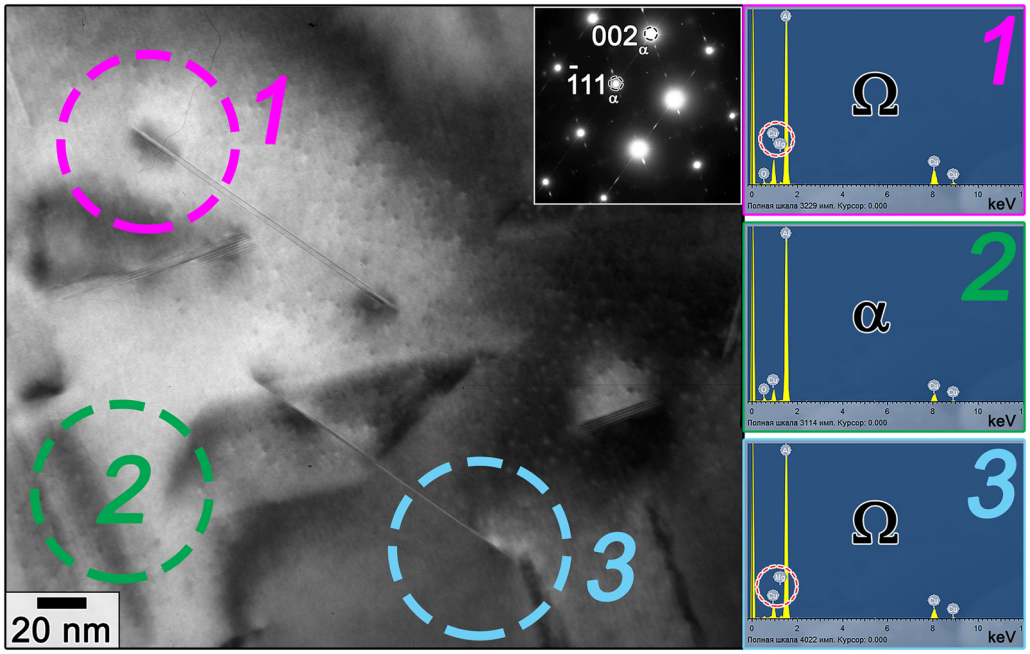

Fig. 11. BF-TEM image and associated SAED pattern taken in $< 011 >_{\alpha}$ zone axes after a pre-strain of 1% followed by ageing at 190 °C for 12 h. EDXS analysis of the matrix (marked with 2) and Ω-phase marked 1 and 3 shows the presence of Mg peaks in both plates. Note the strain fields at the edges. (For interpretation of the references to color in this figure legend, the reader is referred to the web version of this article.)

homogenous nucleation of the θ′-phase with a high AR [5] to the heterogeneous nucleation of this phase with lower AR on the dislocations (Table 4). The thickness of the θ′-phase nucleated on lattice dislocations is lower than that nucleated homogenously (Table 4). The formation energy per Cu solute is lower [43]. This decrease in formation energy is compensated by reducing the total strain energy of the platelet [6]. It is worth noting that changes in the nucleation mechanism of the θ′-phase due to pre-straining affects the number density of this phase and has no impact on its volume fraction. Thus, the pre-straining promotes precipitation of the θ′-phase at the expense of the θ″-phase. These results are broadly in agreement with previous reports [1,9,25,32,49].

The solubility of Mg in the θ′-phase is rather small (approximately ~ 1/50 (in wt%)) and is close to that in the θ-phase [50,51]. As a result, depletion of Mg occurs from the platelets of the θ′-phase precipitated on dislocations, which leads to a significant segregation of Mg atoms near the θ′-phase/Al matrix interfaces [8,42,45,49]. These solute segregations at the interfaces serve as nuclei for the formation of the Ω_{II}-phase in a similar way as Ag segregation aids the formation of the γ′(Al_2Ag)-phase [52]. Agglomerates of the θ′- and Ω_{II}-phases form on lattice dislocations. Thus, nucleation of the θ′-phase on dislocations induces an increase in the number density and volume fraction of the Ω-phase nucleated on the θ′-phase/Al matrix interfaces. As a result, these two phases nucleate and grow almost concurrently, causing two peaks on DSC curve to merge (see Section 3.3) in the AA2519 alloy with low Si. It was recently shown [15] that the free energy of the Ω-phase is higher than that of the θ′-phase. This conclusion is supported by the calculated formation energy of these two phases, reported in works [7,10]. As a result, the Ω_{II}-phase adjacent to the θ′-phase tends to dissolve with increasing ageing time in accordance with well-known the Gibbs-Thomson schema [6] that leads to over-ageing. Herewith a major portion of the Ω_{I}-phase is nucleated homogeneously and has no direct contact with the θ′-platelets, which are nearly retained.

After pre-strains ≥ 3% following precipitation sequences occurs:

$$\text{SSSS} \rightarrow \text{GP zones} \rightarrow \theta''\text{−phase} \rightarrow \theta'\text{−phase} + \Omega_{II}\text{−phase} \rightarrow \theta'\text{−phase} \rightarrow \theta\text{−phase} \quad (3)$$

$$\text{SSSS} \rightarrow \{111\}\ \text{clusters} \rightarrow \Omega_{I}\text{−phase} \rightarrow \theta\text{−phase} \quad (4)$$

Thus, pre-straining slightly modifies the precipitation sequence and strongly affects the distribution of the Ω-phase in the AA2519 alloy [5] due to the transition from homogeneous nucleation of the θ′- and Ω_{I}-phases to heterogeneous nucleation of the θ′- and Ω_{II}-phases on dislocations and θ′-phase/Al interfaces, respectively, with an increased dislocation density. The existence of parallel and independent decomposition sequence (4) is attributed to the superior resistance of the Ω_{I}-phase to coarsening/dissolution at T ≤ 250 °C [30].

4.2. Effect of pre-strain on mechanical properties

The strong interactions between the Mg and Cu solutes and dislocations leads to blocking of the lattice dislocations due to the specific type of solid solution strengthening mechanism associated with the formation of clusters of solute atoms on the lattice dislocations, which requires extra force to ensure dislocation glide [15,28,53]. In addition, blocking of the lattice dislocations requires additional emission of lattice dislocations during tension, providing high dislocation density, even with small strains. The increased dislocation density provides a high value of dislocation strengthening [28,53]. As a result, the yield stress strongly increases and the relative effect of dispersion strengthening under peak ageing conditions decreases with pre-straining. The value of the dislocation strengthening is described by a relationship [28,53]:

$$\sigma_{DS} = \alpha M G b \rho^{1/2}, \quad (5)$$

where $\alpha \sim 0.28$ is a numerical factor representing the dislocation-dislocation interaction strength, M is the Taylor factor ranging from 2.98 to 3.08 (calculated from the EBSD data), G is the shear modulus (25.4 GPa), b is Burgers vector and ρ is the dislocation density. A $\Delta\sigma_{DS}$ increment of 120 MPa with a pre-strain of 7% without ageing was calculated; that is significantly lower than the experimental increment in yield stress (200 MPa). Taking into account that microstructural observations revealed neither change in the grain size nor the formation of deformation bands [28], the efficiency of the solid solution

strengthening attributed to the formation Cu-Mg clouds on dislocations and clustering in Al matrix is ~80 MPa. It is apparent that increasing the pre-strain strongly increases the contribution of this mechanism to the overall σ_{YS}.

T87 tempering produces a high number density of the plate-shaped θ′-precipitates forming on the $\{001\}_\alpha$ planes and Ω-phase precipitates forming on the $\{111\}_\alpha$ planes. These arrays of non-shearable, thick, θ′-platelets and shear-resistant, thin, Ω-phase platelets provide superior mechanical properties of the AA2519T87 alloy. Dislocation strengthening majorly contributes to the increase in σ_{YS} after pre-strains ≥ 3%. The role of increasing number density of the θ′-and Ω-phases is minor. A pre-strain of 7% increases the number density of the θ′-phase and Ω-phase by factors of 15 and ~ 4, respectively. However, these changes in the distribution of shear-resistant secondary phases have little effect on the contribution of dispersion hardening to the overall σ_{YS}. This is attributed to the decreased AR of these phase platelets [20] due to the transition from homogeneous nucleation to heterogeneous one and the insignificant effect of pre-strain on the volume fraction of the θ′-phase. Under peak-ageing, pre-strains ≥ 3% provide full replacement of the shearable θ″-platelets by the shear-resistant θ′- and Ω-phase platelets. As a result, the value of dispersion hardening remains virtually unchanged.

Analysis of the AA2519 alloy under T6 [5] and T87 conditions shows that almost the whole increase of 130 MPa in yield stress can be attributed to the increase in dislocation density by a factor of ~ 12. The increase in dislocation strengthening is 120 MPa. It is worth noting that, we are not able to adequately calculate the lattice dislocation density after peak ageing because the T8-tempered alloy contains the semi-coherent θ′ phase, which forms specifically on dislocations. Accordingly, these precipitates generate matrix coherency strains, which cause broadening of the X-Ray peaks. A small decrease in the density of the lattice dislocations might occur during ageing, but it will decrease the value of dislocation strengthening insignificantly (≤ 25 MPa). Therefore, the value of dispersion strengthening attributed to a dispersion of θ″- and θ′-phases in AA2519T6 and that of the θ′- and Ω-phases in AA2519T87 is nearly the same, despite distinct differences in the dimensions and number density of these platelets.

5. Conclusions

We have investigated the mechanical properties and related phase composition of modern heat-treatable Al–Cu–Mg alloy, processed in T8 temper. Based on the obtained results, the following conclusions can be drawn:

1. A pre-strain of 7% increases the yield stress from 136 to 336 MPa, ultimate tensile strength from 328 to 403 MPa, and decreases the ductility from 27% to 18%. Only half of the change in the yield stress could be attributed to increased dislocation density.
2. Pre-straining hinders the formation of GP-zones and the θ″-phase and strongly promotes precipitation of the θ′-phase on dislocations. Increasing the pre-strain modifies the mechanisms of θ′- and Ω-phase nucleation from homogeneous nucleation to heterogeneous nucleation on dislocations and the θ′-phase/Al matrix interfaces, respectively. Agglomerates consisting of platelets with $\{100\}_{Al}$ and $\{111\}_{Al}$ habit planes nucleate and grow concurrently under peak-ageing.
3. After pre-strains ≥ 3%, the following precipitation sequences occurs:
   SSSS → GP-zones → θ″-phase → θ′-phase + Ω_{II}-phase → θ′-phase → θ-phase and
   SSSS → {111} clusters → Ω_I-phase → θ-phase.
   The Ω_I-phase nucleates homogeneously and exhibits an AR of ~120. The Ω_{II}-phase nucleates on the Al matrix/θ′-phase interfaces and exhibits an AR of ~ 35. Dissolution of the Ω_{II}-phase leads to over-ageing.
4. T87 tempering provides an increase in yield stress from 295 to 422 MPa and in ultimate tensile strength from 409 to 471 MPa, in comparison to T6 temper. The elongation-to-failure decreases slightly. Increase in this dislocation density majorly contributes to the increase in yield stress by thermomechanical processing.

Acknowledgments

This work is supported by the Ministry of Education and Science of the Russian Federation under the agreement №14.584.21.0023 (ID number RFMEFI58417X0023). The authors are grateful to the staff of the Joint Research Center, “Technology and Materials”, Belgorod State National Research University for their assistance with the mechanical and structural characterizations. I.Z. would like to acknowledge Dr. M. Gazizov for helpful and fruitful discussions in the early stages of this work.

References

[1] I. Palmer, D. StJohn, J.-F. Nie, M. Qian, Light Alloys: Metallurgy of the Light Metals, 5th ed., Butterworth-Heinemann, 2017.
[2] I. Crouch, The Science of Armour Materials, Woodhead Publishing, 2016.
[3] I.S. Zuiko, M.R. Gazizov, R.O. Kaibyshev, Effect of thermomechanical treatment on the microstructure, phase composition, and mechanical properties of Al–Cu–Mn–Mg–Zr alloy, Phys. Met. Metallogr. 117 (2016) 906–919.
[4] R.K. Wyss, R.E. Sanders Jr., Microstructure-property relationship in a 2XXX aluminum alloy with Mg addition, Metall. Trans. A 19 (1988) 2523–2530.
[5] I. Zuiko, R. Kaibyshev, Aging behavior of an Al–Cu–Mg alloy, J. Alloy. Compd. 759 (2018) 108–119.
[6] D.A. Porter, K.E. Easterling, M. Sherif, Phase Transformations in Metals and Alloys, 3rd ed., CRC Press, 2009.
[7] S.C. Wang, M.J. Starink, Precipitates and intermetallic phases in precipitation hardening Al–Cu–Mg–(Li) based alloys, Int. Mater. Rev. 50 (2005) 193–215.
[8] S.P. Ringer, B.T. Sofyan, K.S. Prasad, G.C. Quan, Precipitation reactions in Al–4.0Cu–0.3Mg (wt%) alloy, Acta Mater. 56 (2008) 2147–2160.
[9] M. Gazizov, R. Kaibyshev, Effect of pre-straining on the aging behavior and mechanical properties of an Al–Cu–Mg–Ag alloy, Mater. Sci. Eng. A 625 (2015) 119–130.
[10] S.J. Kang, Y.-W. Kim, M. Kim, J.-M. Zuo, Determination of interfacial atomic structure, misfits and energetics of Ω phase in Al–Cu–Mg–Ag alloy, Acta Mater. 81 (2014) 501–511.
[11] Y. Chen, Z. Zhang, Z. Chen, A. Tsalanidis, M. Weyland, S. Findlay, L.J. Allen, J. Li, N.V. Medhekar, L. Bourgeois, The enhanced theta-prime (θ′) precipitation in an Al-Cu alloy with trace Au additions, Acta Mater. 125 (2017) 340–350.
[12] G.B. Winkelman, K. Raviprasad, B.C. Muddle, Stimulation of the Ω-phase in an Al–1.1 at% Cu–0.5 at%Mg alloy by a duplex ageing treatment involving initial natural ageing, Philos. Mag. Lett. 85 (2005) 193–201.
[13] D. Bakavos, P.B. Prangnell, B. Bes, F. Eberl, The effect of silver on microstructural evolution in two 2xxx series Al-alloys with a high Cu:Mg ratio during ageing to a T8 temper, Mater. Sci. Eng. A 491 (2008) 214–223.
[14] N. Ünlü, B.M. Gable, G.J. Shiflet, E.A. Starke Jr., The effect of cold work on the precipitation of Ω and θ′ in a ternary Al–Cu–Mg alloy, Metall. Mater. Trans. A 34 (2003) 2757–2769.
[15] M. Gazizov, R. Kaibyshev, Precipitation structure and strengthening mechanisms in an Al–Cu–Mg–Ag alloy, Mater. Sci. Eng. A 702 (2017) 29–40.
[16] L. Liu, J.H. Chen, S.B. Wang, C.H. Liu, S.S. Yang, C.L. Wu, The effect of Si on precipitation in Al–Cu–Mg alloy with a high Cu/Mg ratio, Mater. Sci. Eng. A 606 (2014) 187–195.
[17] J.Z. Liu, S.S. Yang, S.B. Wang, J.H. Chen, C.L. Wu, The influence of Cu/Mg atomic ratios on precipitation scenarios and mechanical properties of Al–Cu–Mg alloys, J. Alloy. Compd. 613 (2014) 139–142.
[18] Z. Gao, X. Zhang, M. Chen, Investigation on θ′ precipitate thickening in 2519A-T87 aluminum alloy plate impacted, J. Alloy. Compd. 476 (2009) L1–L3.
[19] W. Wang, X. Zhang, Z. Gao, Y. Jia, L. Ye, D. Zheng, L. Liu, Influences of Ce addition on the microstructures and mechanical properties of 2519A aluminum alloy plate, J. Alloy. Compd. 491 (2010) 366–371.
[20] J. da Costa Teixeira, D.G. Cram, L. Bourgeois, T.J. Bastow, A.J. Hill, C.R. Hutchinson, On the strengthening response of aluminum alloys containing shear-resistant plate-shaped precipitates, Acta Mater. 56 (2008) 6109–6122.
[21] L. Bourgeois, C. Dwyer, M. Weyland, J.-F. Nie, B.C. Muddle, The magic thicknesses of θ′ precipitates in Sn-microalloyed Al–Cu, Acta Mater. 60 (2012) 633–644.
[22] J.F. Nie, B.C. Muddle, Strengthening of an Al–Cu–Sn alloy by deformation-resistant precipitate plates, Acta Mater. 56 (2008) 3490–3501.
[23] Z.Q. Liao, Z.Q. Zheng, S.C. Li, W.Q. Liu, B. Cai, S. Zhong, Nanoscale precipitation in aged Al–3.5Cu–0.4Mg–0.2Ge alloy, Mater. Sci. Eng. A 583 (2013) 210–219.
[24] S. Abis, P. Mengucci, G. Riontino, Influence of Si additions on the ageing process of an Al–Cu–Mg–Ag alloy, Philos. Mag. A 70 (1994) 851–868.
[25] A.K. Mukhopadhyay, Coprecipitation of Ω and σ phases in Al–Cu–Mg–Mn alloys containing Ag and Si, Metall. Mater. Trans. A 33 (2002) 3635–3648.
[26] E. Gariboldi, P. Bassani, M. Albu, F. Hofer, Presence of silver in the strengthening

particles of an Al–Cu–Mg–Si–Zr–Ti–Ag alloy during severe overaging and creep, Acta Mater. 125 (2017) 50–57.
[27] V. Fallah, B. Langelier, N. Ofori-Opoku, B. Raeisinia, N. Provatas, Sh Esmaeili, Cluster evolution mechanisms during aging in Al–Mg–Si alloys, Acta Mater. 103 (2016) 290–300.
[28] I. Zuiko, R. Kaibyshev, Deformation structures and strengthening mechanisms in an Al–Cu alloy subjected to extensive cold rolling, Mater. Sci. Eng. A 702 (2017) 53–64.
[29] A. Garg, J.M. Howe, Nucleation and growth of Ω phase in Al–4.0 Cu–0.5 Mg–0.5 Ag alloy – an *in situ* hot-stage TEM study, Acta Metall. Mater. 39 (1991) 1925–1937.
[30] C.R. Hutchinson, X. Fan, S.J. Pennycook, G.J. Shiflet, On the origin of the high coarsening resistance of Ω plates in Al–Cu–Mg–Ag alloys, Acta Mater. 49 (2001) 2827–2841.
[31] S. Bai, P. Ying, Z. Liu, J. Wang, J. Li, Quantitative transmission electron microscopy and atom probe tomography study of Ag-dependent precipitation of Ω phase in Al–Cu–Mg alloys, Mater. Sci. Eng. A 687 (2017) 8–16.
[32] X.Q. Zhao, M.J. Shi, J.H. Chen, S.B. Wang, C.H. Liu, C.L. Wu, A facile electron microscopy method for measuring precipitate volume fractions in AlCuMg alloys, Mater. Charact. 69 (2012) 31–36.
[33] D.B. Williams, C.B. Carter, Transmission Electron Microscopy: A Textbook for Materials Science, 3rd ed., Springer, New York, 2009.
[34] Military Handbook Metallic Materials and Elements for Aerospace Vehicle Structures MIL-HDBK-5H, Department of Defense, December p. 3-164.
[35] D. Tabor, The Hardness of Metals, Clarendon Press, Oxford, 1951.
[36] D. Yuzbekova, A. Mogucheva, D. Zhemchuzhnikova, T. Lebedkina, M. Lebyodkin, R. Kaibyshev, Effect of microstructure on continuous propagation of the Portevin-Le Chatelier deformation bands, Int. J. Plast. 96 (2017) 210–226.
[37] S.D. Antolovich, R.W. Armstrong, Plastic strain localization in metals: origins and consequences, Prog. Mater. Sci. 59 (2014) 1–160.
[38] M. Jobba, R.K. Mishra, M. Niewczas, Flow stress and work-hardening behaviour of Al–Mg binary alloys, Int. J. Plast. 65 (2015) 43–60.
[39] A. Mogucheva, D. Yuzbekova, R. Kaibyshev, T. Lebedkina, M. Lebyodkin, Effect of Grain Refinement on Jerky Flow in an Al–Mg–Sc Alloy, Metall. Mater. Trans. A 47 (2016) 2093–2106.
[40] T.J. Konno, K. Hiraga, M. Kawasaki, Guinier-preston (GP) zone revisited: atomic level observation by HAADF-TEM technique, Scr. Mater. 44 (2001) 2303–2307.
[41] M. Karlík, B. Jouffrey, High resolution electron microscopy study of Guinier-Preston (GP1) zones in Al–Cu based alloys, Acta Mater. 45 (1997) 3251–3263.
[42] Z.Q. Zheng, W.Q. Liu, Z.Q. Liao, S.P. Ringer, G. Sha, Solute clustering and solute nanostructures in an Al–3.5Cu–0.4Mg–0.2Ge alloy, Acta Mater. 61 (2013) 3724–3734.
[43] L. Bourgeois, Ch Dwyer, M. Weyland, J.-F. Nie, B.C. Muddle, Structure and energetics of the coherent interface between the θ′ precipitate phase and aluminium in Al–Cu, Acta Mater. 59 (2011) 7043–7050.
[44] S. Wenner, C.D. Marioara, S.J. Andersen, M. Ervik, R. Holmestad, A hybrid aluminium alloy and its zoo of interacting nano-precipitates, Mater. Charact. 106 (2015) 226–231.
[45] L. Kovarik, S.A. Court, H.L. Fraser, M.J. Mills, GPB zones and composite GPB/GPBII zones in Al–Cu–Mg alloys, Acta Mater. 56 (2008) 4804–4815.
[46] S.C. Wang, M.J. Starink, Two types of S phase precipitates in Al–Cu–Mg alloys, Acta Mater. 55 (2007) 933–941.
[47] A. Biswas, D.J. Siegel, C. Wolverton, D.N. Seidman, Precipitates in Al–Cu alloys revisited: Atom-probe tomographic experiments and first-principles calculations of compositional evolution and interfacial segregation, Acta Mater. 59 (2011) 6187–6204.
[48] E. Gumbmann, W. Lefebvre, F. De Geuser, Ch Sigli, A. Deschamps, The effect of minor solute additions on the precipitation path of an Al–Cu–Li alloy, Acta Mater. 115 (2016) 104–114.
[49] R.K.W. Marceau, G. Sha, R. Ferragut, A. Dupasquier, S.P. Ringer, Solute clustering in Al–Cu–Mg alloys during the early stages of elevated temperature ageing, Acta Mater. 58 (2010) 4923–4939.
[50] S. Mondol, T. Alam, R. Banerjee, S. Kumar, K. Chattopadhyay, Development of a high temperature high strength Al alloy by addition of small amounts of Sc and Mg to 2219 alloy, Mater. Sci. Eng. A 687 (2017) 221–231.
[51] M. Gazizov, V. Teleshov, V. Zakharov, R. Kaibyshev, Solidification behaviour and the effects of homogenisation on the structure of an Al–Cu–Mg–Ag–Sc alloy, J. Alloy. Compd. 509 (2011) 9497–9507.
[52] J.M. Rosalie, L. Bourgeois, Silver segregation to θ′ (Al_2Cu)–Al interfaces in Al–Cu–Ag alloys, Acta Mater. 60 (2012) 6033–6041.
[53] S. Malopheyev, R. Kaibyshev, Strengthening mechanisms in a Zr-modified 5083 alloy deformed to high strains, Mater. Sci. Eng. A 620 (2015) 246–252.